

On the Acceleration of the Young Solar Wind from Different Source Regions

YIMING JIAO,^{1,2} YING D. LIU,^{1,2} WENSHUAI CHENG,^{1,2} HAO RAN,³ AND RUI WANG^{1,2}

¹*State Key Laboratory of Space Weather, National Space Science Center, Chinese Academy of Sciences, Beijing, China; liuxying@hotmail.com*

²*University of Chinese Academy of Sciences, Beijing, China*

³*Mullard Space Science Laboratory, University College London, Dorking, RH5 6NT, United Kingdom*

ABSTRACT

The acceleration of the young solar wind is studied using the first 17 encounters of Parker Solar Probe. We identify wind intervals from different source regions: coronal hole (CH) interiors, streamers, and low Mach number boundary layers (LMBLs), i.e. the inner boundaries of coronal holes. We present their statistical trends in the acceleration process. Most of the observations can be reproduced by a two-fluid hydrodynamic model with realistic corona temperatures. In such a model, the solar wind is accelerated by the combined thermal pressures of protons and electrons, but it is mainly the difference in the proton pressure that leads to the difference in the solar wind speed. The proton pressure is the highest in the fastest CH wind, with a high initial proton temperature that decreases slowly. It is lower in the relatively slow LMBL wind, and the lowest in the slowest streamer wind. The proton temperature is quadratically correlated with the wind speed when scaled to the same distance. In contrast, the electron temperature shows no significant differences for different wind types or wind speeds, indicating more similar contributions from the electron pressure. The model gives reasonable locations for the sonic critical point, which is on average at 3.6-7.3 solar radii and can also extend to large distances when the proton temperature is extremely low, as in the

LMBL wind. In addition to the thermal pressure, we raise the possibility that Alfvén waves may contribute to the solar wind acceleration, especially for the fast CH wind.

1. INTRODUCTION

The solar wind acceleration mechanisms have been studied for decades and remain an important topic in solar and space physics. Since the first fluid theory established by [Parker \(1958\)](#), a number of theoretical works have been devoted to explaining how the solar wind is accelerated from the corona (e.g., [Parker 1960](#); [Weber & Davis 1967](#); [Hartle & Sturrock 1968](#); [Lemaire & Scherer 1971](#); [Hollweg 1986](#)). These early works usually focus on reproducing 1 au observations. The launch of the Parker Solar Probe (PSP; [Fox et al. 2016](#)) mission in 2018 has allowed observations of the solar wind at a much closer distance to the Sun than ever before. This provides observational constraints on the radial evolution of the solar wind at its early stage, which allows us to study the acceleration of the young solar wind for the first time.

In the studies of the solar wind acceleration, it is typical to divide the wind into fast and slow wind according to its speed at 1 au and to consider them separately. However, as the solar wind is still accelerating at the close distance of PSP to the Sun, dividing it simply by speeds may cause a mixing of streams. A slow stream near the Sun may be a fast one at 1 au. Several alternative ways have been developed to define the wind families at PSP distances such as the use of the asymptotic speed ([Halekas et al. 2022, 2023](#)), the statistical quantile of speeds ([Maksimovic et al. 2020](#); [Dakeyo et al. 2022](#)), and the correlation of wind speed with proton temperature ([Pierrard & Peters de Bonhome 2024](#)). In any case, the differences in the solar wind speed are ultimately rooted in its source region, with the fast wind coming from inside the coronal holes (e.g., [Nolte et al. 1976](#); [Zirker 1977](#)) and the slow wind mostly thought to come from closed streamers (e.g., [Sheeley et al. 1997](#); [Chen et al. 2009](#)). Recent works have identified another type of slow wind from PSP measurements that originates from coronal hole inner boundaries, termed the low Mach number boundary layer (LMBL) ([Liu et al. 2023b, 2024](#); [Jiao et al. 2024](#); [Ran et al. 2024](#); [Cheng et al. 2024](#)). Rooted in the rapidly diverging open magnetic fields of the coronal hole boundaries, the LMBL wind is characterised by a reduced

Alfvén Mach number and leads directly to the first observed sub-Alfvénic solar wind (Liu et al. 2023b; Jiao et al. 2024), making it a unique component of the pristine solar wind. Jiao et al. (2024) has shown that the fast coronal hole wind, the streamer wind, and the LMBL wind are three main components of the young solar wind. In this study, we divide the young solar wind into three families according to its sources. The acceleration of these wind families can be then studied by their respective statistical trends.

In the hydrodynamic description, the thermal pressure gradient in the young solar wind can cause it to accelerate against the solar gravity. This process was first established by Parker (1958) using a single-fluid, isothermal hydrodynamic model. The model has since been extended in several ways. One is to represent the protons and electrons as two different species with different temperatures (e.g., Hartle & Sturrock 1968; Lemaire & Scherer 1971; Hollweg 1986; Tu & Marsch 1997; Chandran et al. 2011), as the weak interaction between these two species of particles can hardly equalise their temperature. In such models, the electron pressure acts on the protons through an electric field. Another is to revise the isothermal assumption that requires infinite energy injection. Parker (1960) depicted a model in which the corona obtains enough energy to be isothermal within a distance near the Sun and expands adiabatically further away. Other works tried polytropic models where the plasma get a finite amount of heating (e.g., Parker 1964a,b; Keppens & Goedbloed 1999; Shi et al. 2022). More recently, Dakeyo et al. (2022) combined the isothermal and polytropic models into an isopoly model. The model is isothermal out to a certain distance and then followed by a polytropic model, in which the polytropic indices are determined by in-situ measurements. The success of this model in reproducing most of the observations suggests that thermal pressure gradient plays an important role in solar wind acceleration. On this basis, it is necessary to investigate the possible hydrodynamic processes in the three young solar wind families, which may reveal key properties of the solar wind source and acceleration regions.

The proton and electron thermal pressure gradients, which act to accelerate the solar wind in two-fluid hydrodynamic models, are closely related to the proton and electron temperature profiles. However, since the protons and electrons are heated from different sources and mechanisms (e.g.,

Hollweg 1976; Kasper et al. 2013; Kobayashi et al. 2017), their temperatures can be very different in the young solar wind and therefore have separate effects on the solar wind acceleration. This may be reflected in the relationships between the proton and electron temperatures and the velocity. In fact, while the positive correlation between the proton temperature and solar wind speed is well established (e.g., Lopez 1987; Démoulin 2009; Elliott et al. 2012), the relationship between the electron temperature and speed is less clear. Some suggest an anti-correlation (Maksimovic et al. 2020; Halekas et al. 2020; Liu et al. 2023a; Shi et al. 2023), but this often depends on the distance (Maksimovic et al. 2020; Liu et al. 2023a; Shi et al. 2023) or wind speed (Shi et al. 2023). The problem of the temperature-velocity relationship needs to be further discussed for the young solar wind, as it may reveal the roles of proton and electron thermal pressures in the wind acceleration.

In this letter, we focus on the acceleration of the young solar wind and examine how different source regions affect the wind properties. In section 2, we show the classification of the solar wind into three sources, including coronal hole interiors, streamers and coronal hole boundaries, and present the details of the two-fluid isopoly model we use. In section 3 we show the statistical trends of the three wind types and compare them with the modeling results. We also discuss how proton and electron temperatures are correlated to the velocities for the three wind families. The conclusions are summarized in section 4.

2. OBSERVATIONS AND METHODOLOGY

2.1. *Data Classification*

We use PSP in-situ measurements of the first 17 encounters to select solar wind data from different source regions. Parameters of the solar wind protons are from PSP/SWEAP package (Kasper et al. 2016) with a combined fields of view of the Solar Probe Cup (SPC; Case et al. 2020) and the Solar Probe Analyzer-Ions (SPAN-I; Livi et al. 2022). The alpha particle data are also available starting from encounter 4. The magnetic field data are obtained from the measurements of the PSP/FIELDS fluxgate magnetometer instrument (Bale et al. 2016). The electron density and core temperature are derived from quasi-thermal noise (QTN; Moncuquet et al. 2020) measurements. As the velocity

distribution function can be partially out of the field view for some time, the QTN electron density is used as a proxy for the plasma density throughout the study, and the proton temperature should be considered as a lower limit. All parameters are interpolated to 1 minute averages.

As an example of the data selection, Figure 1 shows the measurements from encounter 10. The basic criteria for coronal hole (CH) wind and streamer wind are that CH wind typically has a higher velocity above 350 km/s and a lower normalized density below 10 cm^{-3} , whereas streamer wind has a lower velocity below 300 km/s and a higher normalized density above 10 cm^{-3} . The threshold values are chosen based on the general properties of the solar wind at PSP distances (e.g., Liu et al. 2023b; Jiao et al. 2024). These two types of wind are identified in Figure 1 with corresponding features of the velocity V_R (Figure 1 (b)) and the electron density n_e (Figure 1 (d)). The electron density is normalized to 1au by a $1/r^2$ factor, with r being the heliocentric distance (Figure 1 (a)). Moreover, previous works suggest that a difference in the alpha-to-proton density ratio, determined by the wind sources, induces differences between CH and streamers. In general, n_α/n_p is higher in the fast CH wind than in the slow streamer wind (Aellig et al. 2001; Kasper et al. 2007, 2012; Fu et al. 2018), consistent with the intervals we have identified (Figure 1 (f)). We use n_α/n_p above or below 0.02 as a secondary criterion to identify the CH wind and the streamer wind.

For the identification of the solar wind coming from the coronal hole boundaries, or the LMBL wind, we adopt the criteria originally proposed by Liu et al. (2023b) that include a decreased radial Alfvén Mach number, a reduced density, and a relatively low velocity. We choose intervals where in general V_R is below 350 km/s, n_e is below 10 cm^{-3} , and M_A is lower than its neighboring wind as the LMBL. The radial Alfvén Mach number M_A is given by $V_R\sqrt{\mu n_e m_p}/B$, where μ is the vacuum magnetic permeability, m_p is the proton mass, and B is the magnetic field strength. The identified LMBL intervals are also shown in Figure 1. In these intervals, a decreased M_A (Figure 1 (g)) is naturally resulted from a reduced n_e and a relatively low V_R , as B tends to remain roughly constant (Figure 1 (c)). Moreover, these LMBL intervals are located in a transition region from the CH wind to the streamer wind, which is consistent with their nature as boundary layers.

Based on the above criteria, we identify the solar wind intervals of the three sources from each encounter of PSP measurements. Another effective way to determine the source of a wind interval is to associate it with magnetic connectivity or EUV imaging. However, due to the large amount of data involved in our study, we instead use the given selection criteria for simplicity.

Table 1 lists the time durations of the three types of wind we identified from each encounter so far. Encounter 8 is not included due to a lack of QTN measurements of the electron core temperature, and encounter 11 is not included due to a lack of QTN data at all. We are cautious with the CH and streamer intervals for the first three encounters, as the alpha particle density is not available and cannot be used as a selection criterion. The total durations of the three types of wind are summarized in the last row of Table 1. These durations are hundreds of hours for each wind type and cover the young solar wind from 14 to 54 solar radii, providing a statistical basis for studying the radial evolution of the young solar wind.

2.2. Two-fluid Isopoly Model

We investigate the possible hydrodynamic processes using a spherically symmetric two-fluid isopoly model, similar to those of [Dakeyo et al. \(2022\)](#) and [Shi et al. \(2022\)](#). The equations of conservation of mass and momentum are

$$n_e V_R r^2 = \text{constant}, \quad (1)$$

$$V_R \frac{dV_R}{dr} = -\frac{1}{n_e m_p} \sum_{s=p,e} \frac{dP_s}{dr} - \frac{GM}{r^2}, \quad (2)$$

where P_s is the pressure of the particle species s , which is either protons p or electrons e , G is the gravitational constant, and M is the solar mass. The pressure P_s is related to the temperature T_s by the ideal gas law $P_s = n_e k_B T_s$, where k_B is the Boltzmann constant. Integrating Equation 2 from a given point r_0 to any point r we have

$$\frac{1}{2}[V_R(r)^2 - V_R(r_0)^2] = \sum_{s=p,e} \Delta W_s + GM\left(\frac{1}{r} - \frac{1}{r_0}\right), \quad (3)$$

where ΔW_s is the work per unit mass done by the pressure gradient force of species s from r_0 to r . For each particle species s , the isopoly model contains an isothermal regime in the solar vicinity

out to the distance $r_{\text{iso},s}$ and a polytropic regime further away. In the isothermal regime $r < r_{\text{iso},s}$, the temperature $T_s(r) = T_s(r_0)$ is constant and the pressure gradient can be written as

$$\frac{dP_s}{dr} = k_B T_s(r_0) \frac{dn_e}{dr}. \quad (4)$$

In the polytropic regime $r > r_{\text{iso},s}$, the polytropic relation gives $T_s n_e^{-(\gamma_s-1)} = \text{constant}$, where $\gamma_s > 1$ is the polytropic index, and $\gamma_s = 1$ corresponds to the isothermal case. In the form of the power-law evolution $T_s \propto r^{\alpha_s}$ and $n_e \propto r^\beta$, the polytropic index is calculated as $\gamma_s = 1 + \alpha_s/\beta$. The pressure gradient is then obtained using the polytropic relation as

$$\frac{dP_s}{dr} = \frac{\gamma_s}{\gamma_s - 1} n_e k_B \frac{dT_s}{dr}, \quad (5)$$

Plugging Equation 4 and Equation 5 into the pressure gradient term of Equation 2 and integrating it, in combination with the polytropic relation and Equation 1, we get

$$\Delta W_s = \begin{cases} -c_s(r_0)^2 \ln\left[\frac{V_R(r_0) r_0^2}{V_R(r) r^2}\right], & \gamma_s = 1 \\ -\frac{c_s(r_0)^2}{(\gamma_s - 1)} \left(\left[\frac{V_R(r_0) r_0^2}{V_R(r) r^2}\right]^{\gamma_s-1} - 1\right), & \gamma_s > 1, \end{cases} \quad (6)$$

where $c_s(r_0)^2 = \gamma_s k_B T_s(r_0)/m_p$ is the square of the equivalent sound speed of species s at r_0 . This means that in any regime of the isopoly model, as long as $T_s(r_0)$ and $V_R(r_0)$ at a given point r_0 are known, the velocity $V_R(r)$ at any other point r can be solved from Equation 3 and Equation 6. Then $n_e(r)$ is given by Equation 1 and $T_s(r)$ is given by the polytropic relation.

Since the protons and electrons transit from isothermal to polytropic at different distances $r_{\text{iso},p}$ and $r_{\text{iso},e}$, the model actually contains three layers. The first layer is the isothermal regime for both species that $\gamma_p = \gamma_e = 1$. In this case, Equation 3 and Equation 6 can be simplified to the isothermal solar wind model in Parker (1958) that passes through a singular point

$$r_c = \frac{GM}{2V_c^2} \quad \text{and} \quad V_c^2 = \frac{k_B (T_{p0} + T_{e0})}{m_p}, \quad (7)$$

which serves as the known point r_0 when the initial temperatures T_{p0} and T_{e0} are given. The point r_c is the sonic critical point where the solar wind transitions from subsonic to supersonic, and V_c

is the wind speed at r_c . We set initial temperature T_{s0} and isothermal distance $r_{\text{iso},s} > r_c$ for each species s as the input parameters. We assume that the sonic critical point occurs in the first layer (see [Dakeyo et al. 2022](#)). Then the first layer of the model is solved with r_c as the given point. The second layer is isothermal for one species and polytropic for the other. For example, if $r_{\text{iso},p} < r_{\text{iso},e}$, the second layer is characterized as $r_{\text{iso},p} < r < r_{\text{iso},e}$, $\gamma_e = 1$, and $\gamma_p > 1$. Since the model is continuous, this layer can be solved by using $r_{\text{iso},p}$, the end point of the previously solved layer, as the known point r_0 . The last layer in our example has $r > r_{\text{iso},e}$, and it is polytropic for both species. It can be solved by using the end point of the second layer $r_{\text{iso},e}$ as r_0 . Thus we have a complete set of profiles of V_R , n_e , T_p and T_e relative to r given by the model.

3. COMPARISON BETWEEN OBSERVATIONS AND MODEL

Figure 2 presents the variations of velocity V_R , density n_e , proton temperature T_p and electron temperature T_e as a function of heliocentric distance r . We bin the data every five solar radii and calculate the mean values and standard deviations of r and of each parameter. These values are shown as data points and error bars. We notice an inconsistency between the T_p values measured by SPC and by SPAN-I that T_p from SPC is much lower. This could be explained by the fact that the SPC measurements are dominated by the core of the proton distribution function, while the SPAN-I measurements also include the nonthermal component ([Dakeyo et al. 2022](#)). As SPAN-I measurements alone can cover most of the radial range during the encounters, only T_p from SPAN-I is used in the following study.

We first fit the data points with a power-law function to describe their trends empirically. For n_e , T_p and T_e , such a form is efficient in describing the expansion process. For V_R , it is used to represent the acceleration of the solar wind, which is rapid near the Sun and then slower further away. We set the acceleration to start from the solar surface. The fitted formulas are shown in Figure 2, but their associated curves are not. The fitted expressions for V_R show the acceleration for the three wind types, and the contrast between the fast wind coming from CHs, the slow wind coming from streamers and the LMBL wind, with the streamer wind being the slowest. The CH wind here is below the typical speed of the fast wind at 1 au, because the wind is still accelerating near the Sun.

Also, the wind coming from the central parts of large coronal holes is rarely measured by PSP so far. The lower speed limit set in the CH wind selection criteria may also have a small effect on this result. The fitting of n_e shows trends that do not deviate far from the spherical expansion of $n_e \propto r^{-2}$, and its values are lower for the CH and LMBL wind than for the streamer wind. As for T_p , it decreases with r at different rates for the three wind types: most rapidly for the streamer wind, slower for the LMBL wind, and slowest for the CH wind. The initial values in the fitting are similar for the three wind types. However, as the trends may not extend to the Sun, they cannot be regarded as true coronal values. The expressions for T_e are consistent with the previously estimated $T_e \propto r^{-0.74}$ trend (Moncuquet et al. 2020), and show no significant differences between different wind types. Both T_p and T_e decrease slower than an adiabatic expansion $T \propto r^{-4/3}$ for all wind types, suggesting universal heating in the near-Sun environment.

The profiles given by our isopoly model that fit the measured data point are also shown in Figure 2. For each wind type, given the power-law indices for T_p , T_e and n_e from in situ fitting, the polytropic indices γ_p and γ_e are obtained. The initial temperatures T_{p0} and T_{e0} and the isothermal distances $r_{\text{iso},p}$ and $r_{\text{iso},e}$ are manually adjusted to fit the data. Since $r_{\text{iso},s}$ depends on T_{s0} to ensure a continuous transition from isothermal to polytropic, the only free parameters are T_{p0} and T_{e0} . Most of the observations can be reproduced with realistic parameters, except for the CH wind beyond 40 solar radii (Figure 2 (a)), where the model predicts a slightly lower V_R than the measurements. This discrepancy suggests the possibility of an acceleration mechanism other than the thermal pressure in the CH wind. The sonic critical point r_c and the critical speed V_c are given by the initial temperatures using Equation 7. The Alfvén critical point r_A , which is the point where the Alfvén speed $V_A = B/\sqrt{\mu n_e m_p}$ equals the solar wind speed V_R , is determined by finding the intersection of the two curves of V_R and V_A , where V_R and n_e are obtained from the model and B is from a power-law fitting of the measurements.

Table 2 summarises the model parameters for the three wind types that relate to the profiles in Figure 2. The proton polytropic index γ_p is the smallest for the CH wind at 1.18 and the largest for the streamer wind at 1.35, with the LMBL wind in between at 1.30. The much lower γ_p for the CH

wind suggests that the CH wind is most approximate to isothermal and obtains most heating and acceleration. The initial proton temperatures T_{p0} varies from 0.5 Mk to 2.0 Mk, with the streamer wind having the lowest value and the CH wind the highest. Both small γ_p and high T_{p0} produce a higher T_p profile and greater acceleration in the CH wind, making it faster than the streamer and LMBL wind (see Figure 2). On the contrary, for electrons both the polytropic indices γ_e , which are about 1.36, and the initial temperatures T_{e0} , which are a little more than 1 Mk, are similar for the three wind types. This yields similar T_e profiles for the three wind types as is the case of the fitted power-law expressions (see Figure 2). These results suggest that it is mainly the differences in the proton temperatures that cause the different speeds for different wind types. The sonic critical point positions r_c are slightly higher than previous estimations (e.g., [Habbal et al. 1995](#); [Sheeley et al. 1997](#); [Vásquez et al. 2003](#)). Specifically, according to Equation 7, r_c is closer to the Sun at higher temperatures, so in general the CH wind has the smallest r_c and the streamer wind the largest. This pattern can sometimes be broken, as the LMBL wind can have an extremely low proton temperature and thus an extremely extended r_c ([Liu et al. 2024](#); [Cheng et al. 2024](#)). The Alfvén critical points r_A are around 12 solar radii for the CH wind and the streamer wind, and rise to over 20 solar radii for the LMBL wind, consistent with estimations from PSP in situ measurements ([Liu et al. 2021, 2023b](#); [Jiao et al. 2024](#)).

We further investigate the roles of proton and electron temperatures in solar wind acceleration by looking at their relationships with the velocities. To eliminate the effects of radial variations in velocity and temperatures, we scale V_R , T_p and T_e to $14 R_S$, the outermost isothermal distance of the isopoly model, with the previously fitted power-law functions. We bin the data every 50 km/s of V_R and calculate the mean values and standard deviations of V_R , T_p and T_e within each bin. The results are shown in Figure 3. The scaled T_p is positively correlated with V_R , as expected from the intuition that a higher temperature produces more acceleration. This positive correlation can be described by a quadratic function for all the three wind types as shown in Figure 3, which implies a linear relationship between the thermal energy and kinetic energy. On the other hand, the scaled T_e is around a constant value of 0.7 MK independent of V_R . It appears that after removing the effects

of the radial variations in V_R and T_e , the electron temperature is approximately the same for each wind speed and wind type. The difference in the relationships of T_p and T_e to V_R is also shown in the in situ measurements in Figure 1 (e), where T_p varies significantly with V_R but T_e does not. This again suggests that, as the electron thermal pressure contributes similarly to the acceleration of all solar winds, it is mainly the proton pressure that determines the differences in the wind speed. In general, the CH wind has the highest T_p and V_R values, the streamer wind has the lowest, and r_c is in the same order from the closest to farthest. However, the variation in the T_p and V_R of the LMBL wind is so large that they can reach extremely low values as marked in Figure 3. This can lead to an extremely extended r_c in some LMBL winds. This corresponds to the first observed near-subsonic LMBL wind featuring an extremely low velocity and an extremely low proton temperature (Liu et al. 2024; Cheng et al. 2024).

Accelerating the solar wind requires energy from a variety of sources. Halekas et al. (2023) quantified the energy budget and found that the electric field and Alfvén waves provide enough energy to accelerate the slow and fast solar winds. We repeat their procedures for the three types of wind and get consistent results on the energy budget (not shown here). In the acceleration of the streamer wind, the electric field, which is equivalent to the electron pressure gradient (see Parker 2010), provides most of the energy required. This is also reflected in Table 2 that T_{e0} is much higher than T_{p0} for the streamer wind and LMBL wind. Figure 3 also suggests that the slower the wind, the higher T_e than T_p . In the CH wind, in addition to the electric field, the Alfvén waves can provide the extra kinetic energy as needed for further acceleration. Alfvén waves can both heat the protons and directly accelerate the solar wind (e.g., Hollweg 1973). This may explain the greater heating in the CH wind protons, as indicated by the higher T_{p0} and lower γ_p as well as the additional acceleration in the CH wind that the model cannot produce. Alfvén wave energy is also present in the LMBL wind acceleration, although to a lesser extent than in the CH wind.

4. CONCLUSIONS

We have studied the acceleration of the young solar wind from different source regions using the first 17 encounters of PSP measurements. We identify the CH wind, the streamer wind, and the LMBL

wind as the three main components of the young solar wind, and analyze their statistical trends in the velocity, density, and proton and electron temperatures with distance. The main conclusions are as follows:

1. The acceleration process of the three types of solar wind can mostly be described by a two-fluid isothermal model. The velocity and density profiles, which are consistent with the previously proposed fast and tenuous CH wind, slow and dense streamer wind, and relatively slow but tenuous LMBL wind (Liu et al. 2023b; Jiao et al. 2024), suggest a near-spherical expansion with a small amount of acceleration in the range of the PSP encounter measurements. The proton and electron temperature profiles show a polytropic decrease with distance. When appropriate isothermal layers are added before the polytropic region (Dakeyo et al. 2022; Shi et al. 2022), the proton and electron thermal pressures provided by such temperature profiles are sufficient to reproduce most of the observed velocities by a hydrodynamic mechanism. The streamer and LMBL wind can be fully generated with realistic initial corona temperatures, and the CH wind can be largely explained except for a slightly additional accelerated part beyond 40 solar radii. This indicates the important role of thermal pressure in accelerating the solar wind.
2. The proton and electron temperatures and their corresponding thermal pressures have different effects on the acceleration of the young solar wind. The difference in the proton thermal pressure is primarily responsible for the difference in the wind speed. For the fast CH wind, both a high initial temperature and a subsequent small polytropic index indicate more heating of the protons than in other wind types, and thus more proton pressure contributing to the acceleration. In comparison, the proton pressure that can accelerate the relatively slow LMBL wind is much less, as indicated by a lower initial temperature and a larger polytropic index, and the proton pressure that can accelerate the slowest streamer wind is the least. This is also supported by the positive correlation between the scaled proton temperature and wind speed, which can be described by a quadratic function that holds for all wind types. In contrast, the electron thermal pressure in our results shows less difference in its contribution to the acceleration for

different wind types. This is observed in the similar electron initial temperatures and similar electron polytropic indices for all wind types. In addition, the electron temperature is roughly the same regardless of the wind speed or wind type when scaled to the same distance. If there is no scaling, the radially increasing velocity and the decreasing electron temperature may exhibit an anti-correlation, which should diminish when the measurements are made over a short distance or at a location far enough away that the wind speed is no longer increasing. The different roles of the proton and electron temperatures in the solar wind acceleration may be due to separate heating processes for the two species in the corona. This may require more detailed investigation in the future.

3. The model gives reasonable positions of the sonic critical point and the Alfvén critical point. The position of the sonic critical point is determined by the proton and electron temperatures together. The higher the temperatures, the closer the sonic critical point to the Sun. Since the electron temperatures are similar, the critical point positions of the three wind types are generally in the descending order of the proton temperatures, i.e. first the CH wind at $3.6 R_S$, then the LMBL wind at $6.2 R_S$, and finally the streamer wind at $7.3 R_S$. However, since the proton temperature of the LMBL wind can also reach very low values, its critical point can extend to large distances and even be detected by PSP (Liu et al. 2024; Cheng et al. 2024). We also obtain the position of the Alfvén critical point consistent with previous estimations, which is about 12 solar radii for the CH wind and the streamer wind, but over 20 solar radii for the LMBL wind (Liu et al. 2023b; Jiao et al. 2024).
4. The acceleration of different types of wind is driven by energy from different sources. The slow solar wind, especially the streamer wind, where the proton pressure contributes little to the acceleration, is mainly driven by the electron pressure. In this case, the electrons act on the solar wind through an electric field, which converts the electrical potential energy of the solar wind into kinetic energy. On the other hand, in the CH wind, where the proton pressure contributes more to the acceleration, another source of energy can heat the protons and thus accelerate

the solar wind. The Alfvén waves abundant in the CH wind are a promising candidate, as the energy they contain is sufficient for the acceleration (Halekas et al. 2023). Moreover, the Alfvén waves can directly accelerate the solar wind in addition to heating the protons, which may be relevant for the additional acceleration in the CH wind beyond 40 solar radii. The fewer Alfvén waves in the LMBL wind may also act to heat the protons and accelerate them to higher speeds than in the streamer wind. The role of the Alfvén waves is a potentially helpful point to consider in further refinement of the model.

The research was supported by the Strategic Priority Research Program of the Chinese Academy of Sciences (No.XDB 0560000), by NSFC under grant 12073032, by the National Key R&D Program of China No. 2022YFF0503800 and No. 2021YFA0718600, and by the Specialized Research Fund for State Key Laboratories of China. H.R. is supported by a studentship from the UK Science and Technology Facilities Council (STFC). We acknowledge the NASA Parker Solar Probe mission and the SWEAP and FIELDS teams for the use of data.

REFERENCES

- Aellig, M. R., Lazarus, A. J., & Steinberg, J. T. 2001, *Geophys. Res. Lett.*, 28, 2767, doi: [10.1029/2000GL012771](https://doi.org/10.1029/2000GL012771)
- Bale, S. D., Goetz, K., Harvey, P. R., et al. 2016, *SSRv*, 204, 49, doi: [10.1007/s11214-016-0244-5](https://doi.org/10.1007/s11214-016-0244-5)
- Case, A. W., Kasper, J. C., Stevens, M. L., et al. 2020, *ApJS*, 246, 43, doi: [10.3847/1538-4365/ab5a7b](https://doi.org/10.3847/1538-4365/ab5a7b)
- Chandran, B. D. G., Dennis, T. J., Quataert, E., & Bale, S. D. 2011, *ApJ*, 743, 197, doi: [10.1088/0004-637X/743/2/197](https://doi.org/10.1088/0004-637X/743/2/197)
- Chen, Y., Li, X., Song, H. Q., et al. 2009, *ApJ*, 691, 1936, doi: [10.1088/0004-637X/691/2/1936](https://doi.org/10.1088/0004-637X/691/2/1936)
- Cheng, W., Liu, Y. D., Ran, H., et al. 2024, *ApJ*, 967, 58, doi: [10.3847/1538-4357/ad3b98](https://doi.org/10.3847/1538-4357/ad3b98)
- Dakeyo, J.-B., Maksimovic, M., Démoulin, P., Halekas, J., & Stevens, M. L. 2022, *ApJ*, 940, 130, doi: [10.3847/1538-4357/ac9b14](https://doi.org/10.3847/1538-4357/ac9b14)
- Démoulin, P. 2009, *SoPh*, 257, 169, doi: [10.1007/s11207-009-9338-5](https://doi.org/10.1007/s11207-009-9338-5)
- Elliott, H. A., Henney, C. J., McComas, D. J., Smith, C. W., & Vasquez, B. J. 2012, *Journal of Geophysical Research (Space Physics)*, 117, A09102, doi: [10.1029/2011JA017125](https://doi.org/10.1029/2011JA017125)
- Fox, N. J., Velli, M. C., Bale, S. D., et al. 2016, *SSRv*, 204, 7, doi: [10.1007/s11214-015-0211-6](https://doi.org/10.1007/s11214-015-0211-6)

- Fu, H., Madjarska, M. S., Li, B., Xia, L., & Huang, Z. 2018, *MNRAS*, 478, 1884, doi: [10.1093/mnras/sty1211](https://doi.org/10.1093/mnras/sty1211)
- Habbal, S. R., Esser, R., Guhathakurta, M., & Fisher, R. R. 1995, *Geophys. Res. Lett.*, 22, 1465, doi: [10.1029/95GL01064](https://doi.org/10.1029/95GL01064)
- Halekas, J. S., Whittlesey, P., Larson, D. E., et al. 2020, *ApJS*, 246, 22, doi: [10.3847/1538-4365/ab4cec](https://doi.org/10.3847/1538-4365/ab4cec)
- . 2022, *ApJ*, 936, 53, doi: [10.3847/1538-4357/ac85b8](https://doi.org/10.3847/1538-4357/ac85b8)
- Halekas, J. S., Bale, S. D., Berthomier, M., et al. 2023, *ApJ*, 952, 26, doi: [10.3847/1538-4357/acd769](https://doi.org/10.3847/1538-4357/acd769)
- Hartle, R. E., & Sturrock, P. A. 1968, *ApJ*, 151, 1155, doi: [10.1086/149513](https://doi.org/10.1086/149513)
- Hollweg, J. V. 1973, *ApJ*, 181, 547, doi: [10.1086/152072](https://doi.org/10.1086/152072)
- . 1976, *J. Geophys. Res.*, 81, 1649, doi: [10.1029/JA081i010p01649](https://doi.org/10.1029/JA081i010p01649)
- . 1986, *J. Geophys. Res.*, 91, 4111, doi: [10.1029/JA091iA04p04111](https://doi.org/10.1029/JA091iA04p04111)
- Jiao, Y., Liu, Y. D., Ran, H., & Cheng, W. 2024, *ApJ*, 960, 42, doi: [10.3847/1538-4357/ad0dfc](https://doi.org/10.3847/1538-4357/ad0dfc)
- Kasper, J. C., Maruca, B. A., Stevens, M. L., & Zaslavsky, A. 2013, *PhRvL*, 110, 091102, doi: [10.1103/PhysRevLett.110.091102](https://doi.org/10.1103/PhysRevLett.110.091102)
- Kasper, J. C., Stevens, M. L., Korreck, K. E., et al. 2012, *ApJ*, 745, 162, doi: [10.1088/0004-637X/745/2/162](https://doi.org/10.1088/0004-637X/745/2/162)
- Kasper, J. C., Stevens, M. L., Lazarus, A. J., Steinberg, J. T., & Ogilvie, K. W. 2007, *ApJ*, 660, 901, doi: [10.1086/510842](https://doi.org/10.1086/510842)
- Kasper, J. C., Abiad, R., Austin, G., et al. 2016, *SSRv*, 204, 131, doi: [10.1007/s11214-015-0206-3](https://doi.org/10.1007/s11214-015-0206-3)
- Keppens, R., & Goedbloed, J. P. 1999, *A&A*, 343, 251, doi: [10.48550/arXiv.astro-ph/9901380](https://doi.org/10.48550/arXiv.astro-ph/9901380)
- Kobayashi, S., Sahraoui, F., Passot, T., et al. 2017, *ApJ*, 839, 122, doi: [10.3847/1538-4357/aa67f2](https://doi.org/10.3847/1538-4357/aa67f2)
- Lemaire, J., & Scherer, M. 1971, *J. Geophys. Res.*, 76, 7479, doi: [10.1029/JA076i031p07479](https://doi.org/10.1029/JA076i031p07479)
- Liu, M., Issautier, K., Moncuquet, M., et al. 2023a, *A&A*, 674, A49, doi: [10.1051/0004-6361/202245450](https://doi.org/10.1051/0004-6361/202245450)
- Liu, Y. D., Chen, C., Stevens, M. L., & Liu, M. 2021, *ApJL*, 908, L41, doi: [10.3847/2041-8213/abe38e](https://doi.org/10.3847/2041-8213/abe38e)
- Liu, Y. D., Ran, H., Hu, H., & Bale, S. D. 2023b, *ApJ*, 944, 116, doi: [10.3847/1538-4357/acb345](https://doi.org/10.3847/1538-4357/acb345)
- Liu, Y. D., Zhu, B., Ran, H., et al. 2024, *ApJ*, 963, 85, doi: [10.3847/1538-4357/ad1e56](https://doi.org/10.3847/1538-4357/ad1e56)
- Livi, R., Larson, D. E., Kasper, J. C., et al. 2022, *ApJ*, 938, 138, doi: [10.3847/1538-4357/ac93f5](https://doi.org/10.3847/1538-4357/ac93f5)
- Lopez, R. E. 1987, *J. Geophys. Res.*, 92, 11189, doi: [10.1029/JA092iA10p11189](https://doi.org/10.1029/JA092iA10p11189)
- Maksimovic, M., Bale, S. D., Berčić, L., et al. 2020, *ApJS*, 246, 62, doi: [10.3847/1538-4365/ab61fc](https://doi.org/10.3847/1538-4365/ab61fc)
- Moncuquet, M., Meyer-Vernet, N., Issautier, K., et al. 2020, *ApJS*, 246, 44, doi: [10.3847/1538-4365/ab5a84](https://doi.org/10.3847/1538-4365/ab5a84)

- Nolte, J. T., Krieger, A. S., Timothy, A. F., et al. 1976, *SoPh*, 46, 303, doi: [10.1007/BF00149859](https://doi.org/10.1007/BF00149859)
- Parker, E. N. 1958, *ApJ*, 128, 664, doi: [10.1086/146579](https://doi.org/10.1086/146579)
- . 1960, *ApJ*, 132, 821, doi: [10.1086/146985](https://doi.org/10.1086/146985)
- . 1964a, *ApJ*, 139, 72, doi: [10.1086/147740](https://doi.org/10.1086/147740)
- . 1964b, *ApJ*, 139, 93, doi: [10.1086/147741](https://doi.org/10.1086/147741)
- Parker, E. N. 2010, in *American Institute of Physics Conference Series*, Vol. 1216, Twelfth International Solar Wind Conference, ed. M. Maksimovic, K. Issautier, N. Meyer-Vernet, M. Moncuquet, & F. Pantellini (AIP), 3–7, doi: [10.1063/1.3395887](https://doi.org/10.1063/1.3395887)
- Pierrard, V., & Peters de Bonhome, M. 2024, arXiv e-prints, arXiv:2401.13308, doi: [10.48550/arXiv.2401.13308](https://doi.org/10.48550/arXiv.2401.13308)
- Ran, H., Liu, Y. D., Chen, C., & Mostafavi, P. 2024, *ApJ*, 963, 82, doi: [10.3847/1538-4357/ad2069](https://doi.org/10.3847/1538-4357/ad2069)
- Sheeley, N. R., Wang, Y. M., Hawley, S. H., et al. 1997, *ApJ*, 484, 472, doi: [10.1086/304338](https://doi.org/10.1086/304338)
- Shi, C., Velli, M., Bale, S. D., et al. 2022, *Physics of Plasmas*, 29, 122901, doi: [10.1063/5.0124703](https://doi.org/10.1063/5.0124703)
- Shi, C., Velli, M., Lionello, R., et al. 2023, *ApJ*, 944, 82, doi: [10.3847/1538-4357/acb341](https://doi.org/10.3847/1538-4357/acb341)
- Tu, C. Y., & Marsch, E. 1997, *SoPh*, 171, 363, doi: [10.1023/A:1004968327196](https://doi.org/10.1023/A:1004968327196)
- Vásquez, A. M., van Ballegoijen, A. A., & Raymond, J. C. 2003, *ApJ*, 598, 1361, doi: [10.1086/379008](https://doi.org/10.1086/379008)
- Weber, E. J., & Davis, Leverett, J. 1967, *ApJ*, 148, 217, doi: [10.1086/149138](https://doi.org/10.1086/149138)
- Zirker, J. B. 1977, *RvGSP*, 15, 257, doi: [10.1029/RG015i003p00257](https://doi.org/10.1029/RG015i003p00257)

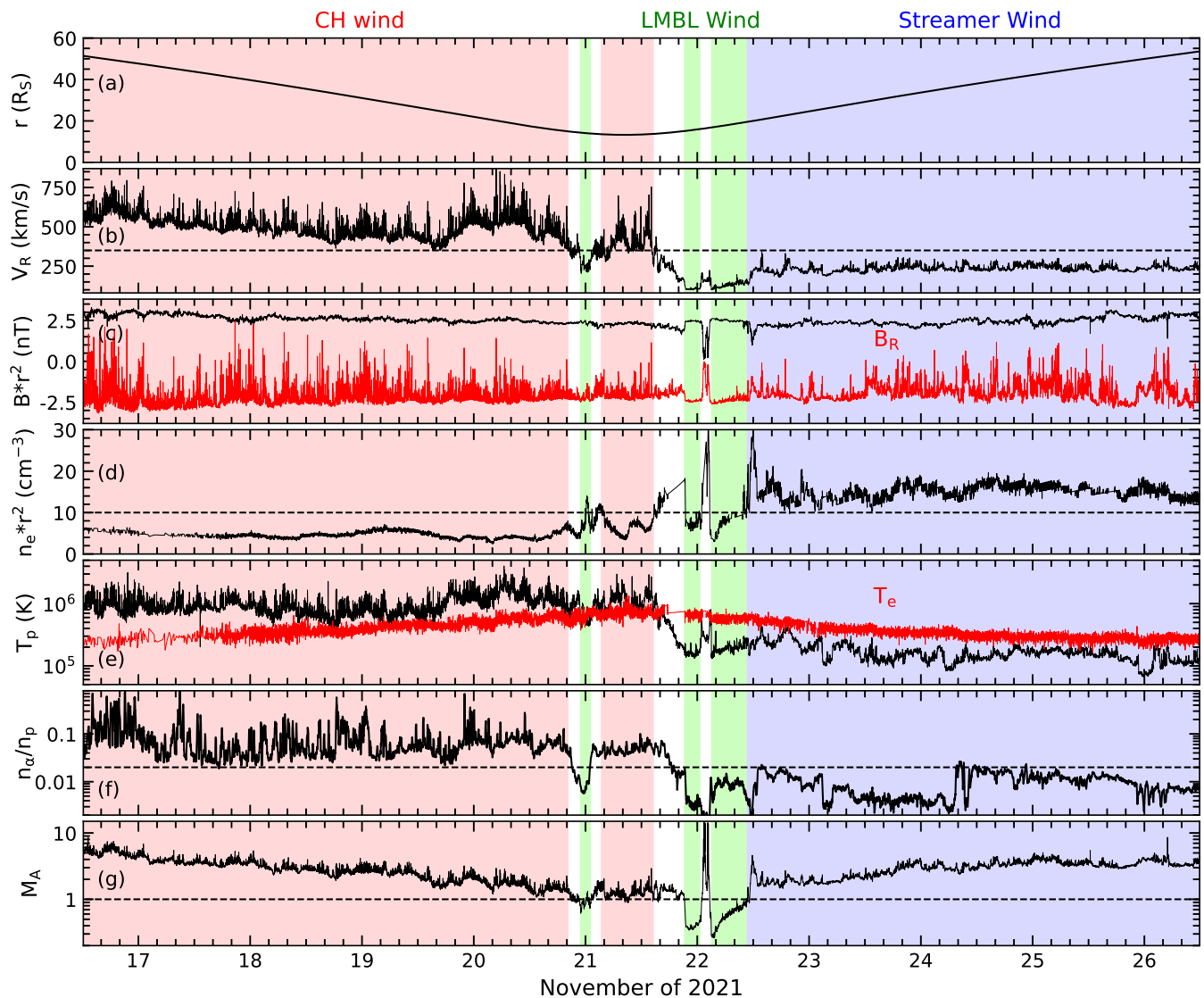


Figure 1. PSP measurements at encounter 10 as an example of data classification. The shaded areas indicate coronal hole wind (red), streamer wind (blue) and LMBL wind (green). (a) PSP heliocentric distance. (b) Proton radial velocity. (c) Magnetic field strength and radial component (red) normalized to 1 AU values. (d) QTN electron density normalized to 1 AU values. (e) Proton temperature and electron core temperature (red). (f) Alpha-to-proton density ratio. The horizontal dashed line marks the value of 0.02. (g) Radial Alfvén Mach number.

Table 1. Durations of Solar Wind Intervals from Different Sources

| Enc. | CH wind (hr) | Streamer wind (hr) | LMBL wind (hr) |
|-------|-----------------|-----------------------|-------------------|
| 1 | 27.7 | 43.2 | 0 |
| 2 | 23.7 | 41.0 | 54.3 |
| 3 | 34.3 | 19.8 | 0 |
| 4 | 57.0 | 116.7 | 10.5 |
| 5 | 6.5 | 47.8 | 11.5 |
| 6 | 46.7 | 6.2 | 19.2 |
| 7 | 45.0 | 131.5 | 4.5 |
| 9 | 33.7 | 23.3 | 12.2 |
| 10 | 115.0 | 97.0 | 12.5 |
| 12 | 104.7 | 51.2 | 43.3 |
| 13 | 112.4 | 10.7 | 27.2 |
| 14 | 130.5 | 29.0 | 21.7 |
| 15 | 71.7 | 0 | 20.2 |
| 16 | 38.8 | 5.5 | 31.0 |
| 17 | 25.7 | 5.5 | 8.3 |
| Total | 817.2 | 635.8 | 280.0 |

NOTE—Durations of the CH wind, streamer wind and LMBL wind identified from the first 17 encounters of PSP measurements. Encounters 8 and 11 are not included due to incomplete or missing QTN measurements.

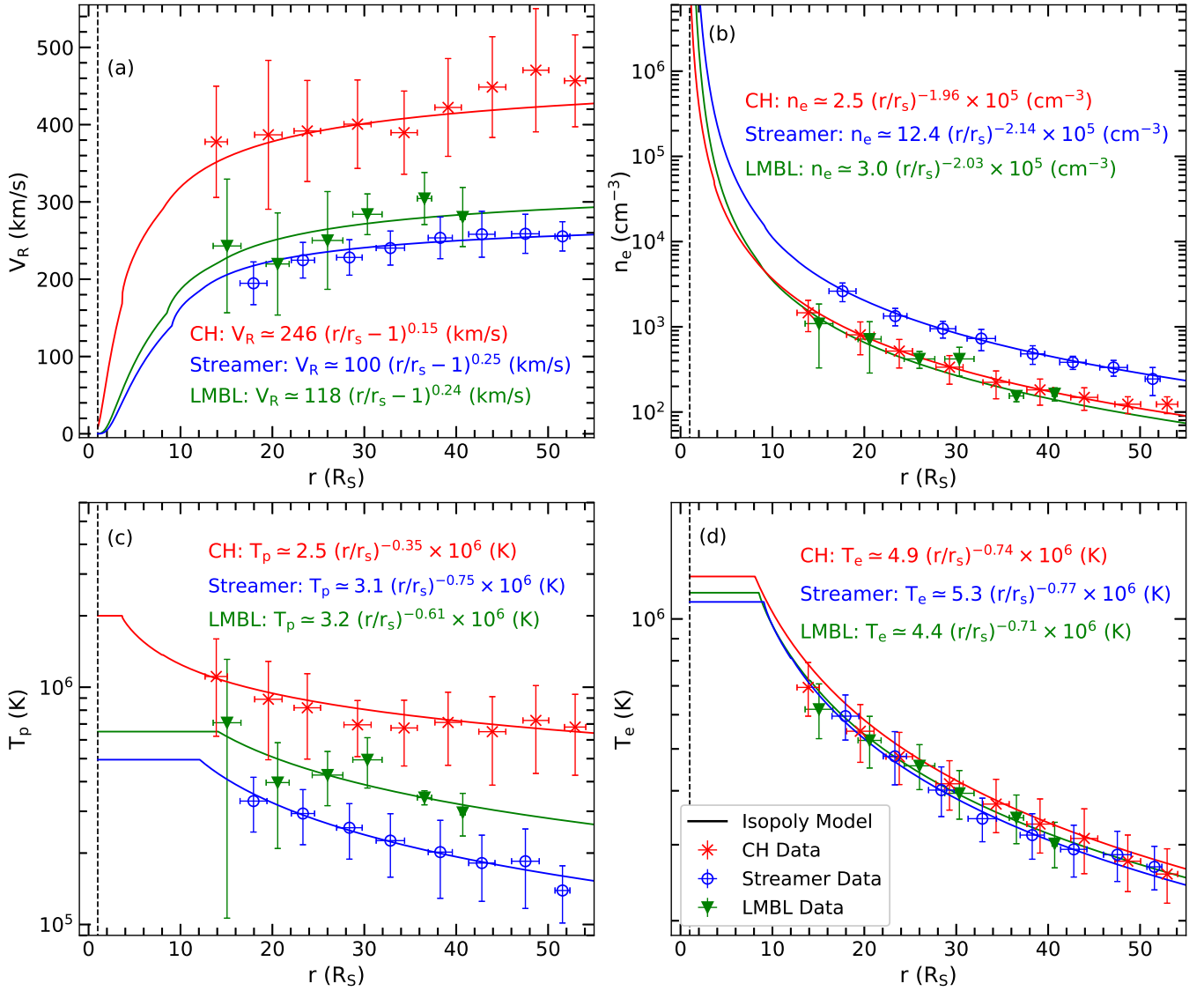


Figure 2. Radial evolution of the solar wind parameters. (a) Radial velocity. (b) Electron density. (c) Proton temperature. (d) Electron temperature. The PSP data are binned every $5 R_S$, and the data points and error bars are the mean values and standard deviations within the bins. The fitted power-law functions are shown as text. The solid lines indicate profiles given by our isopoly model.

Table 2. Parameters Related to the Isopoly Model

| | CH wind | Streamer wind | LMBL wind |
|------------------------------|---------|---------------|-----------|
| α_p | -0.35 | -0.75 | -0.61 |
| α_e | -0.74 | -0.77 | -0.71 |
| β | -1.96 | -2.14 | -2.03 |
| γ_p | 1.18 | 1.35 | 1.30 |
| γ_e | 1.37 | 1.36 | 1.35 |
| T_{p0} (MK) | 2.00 | 0.50 | 0.65 |
| $r_{\text{iso,p}}$ (R_S) | 3.7 | 12.0 | 14.0 |
| T_{e0} (MK) | 1.25 | 1.10 | 1.15 |
| $r_{\text{iso,e}}$ (R_S) | 8.0 | 9.0 | 8.5 |
| r_c (R_S) | 3.6 | 7.3 | 6.2 |
| V_c (km s $^{-1}$) | 164 | 115 | 122 |
| r_A (R_S) | 12.5 | 12.6 | 22.9 |
| V_A (km s $^{-1}$) | 342 | 190 | 258 |

NOTE—Power-law and polytropic indices (top five rows) are obtained by fitting of in situ measurements. Initial temperatures and isothermal distances (middle four rows) are set manually to best fit the data. Critical points and velocities (bottom four rows) are given by the model.

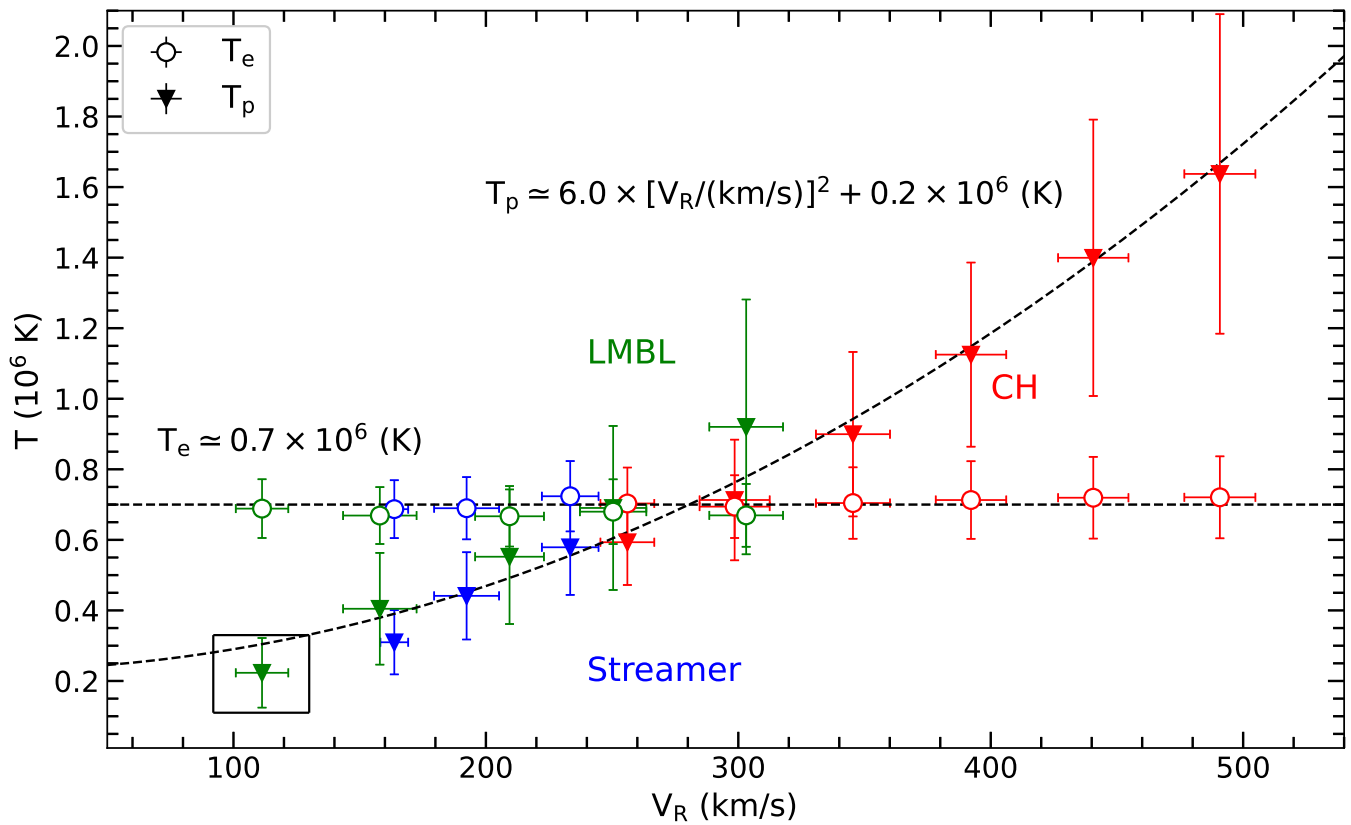


Figure 3. Relationships of proton and electron temperatures with the radial velocity. The V_R , T_p and T_e data are scaled to the same distance ($14 R_S$) and binned every 50 km/s. The dashed lines indicate the fitted functions for protons and electrons, respectively. The box marks the LMBL wind with extremely low velocity and an extremely low proton temperature.